Appl. Phys. A (2014) 117:1977–1984
DOI 10.1007/s00339-014-8605-y

Applied Physics A
Materials Science & Processing

Preparation of *n*-ZnO/*p*-Si solar cells by oxidation of zinc nanoparticles: effect of oxidation temperature on the photovoltaic properties

Raid A. Ismail · Selma M. H. Al-Jawad · Naba Hussein

Received: 14 May 2014 / Accepted: 1 July 2014 / Published online: 11 July 2014

Abstract In this study, *n*-ZnO/*p*-Si solar cells were fabricated by spraying ZnO nanoparticles (NPs) film synthesised by dissolving of high purity zinc in hydrogen peroxide H_2O_2 followed by thermal oxidation in air on *p*-type silicon substrates. The oxidation was carried out at different temperatures (200–500) °C. The crystalline structure of the ZnO NPs films was investigated by X-ray diffraction which indicated wurtzite structure films along (100) plane. The morphology of the NPs was studied by atomic force microscopy and scanning electron microscopy. The result showed an average grain size of ZnO NPs in the range of (72.7–95.8) nm and the surface roughness increasing with oxidation temperature. Three peaks located at ultraviolet, violet and green emission regions were noticed in the photoluminescence spectra of ZnO NPs. From optical studies, it was shown that the direct optical band gap is found to be in the range of (3.85–3.96) eV depended on the oxidation temperature. The synthesised ZnO films have *n*-type conductivity, and the mobility was in the range of (7–24) $cm^2\ V^{-1}\ s^{-1}$. Current–voltage *I*–*V* and capacitance–voltage *C*–*V* of ZnO NPs/Si heterojunction solar cell were investigated as function of oxidation temperature. The spectral response of *n*-ZnO NPs/*p*-Si solar cell showed two peaks of response and its maximum value approaching 0.62 mA W^{-1} at $\lambda = 800$ nm. Solar cell oxidized at 500 °C gave open circuit voltage V_{OC} of 375 mV, short circuit current density J_{SC} of 25 mA cm^{-2}, a fill factor FF of 0.72, and conversion efficiency η of 6.79 % under illumination of 100 mW cm^{-2}.

R. A. Ismail (✉) · S. M. H. Al-Jawad · N. Hussein
Department of Applied Science, University of Technology, Baghdad, Iraq
e-mail: raidismail@yahoo.com

1 Introduction

Semiconductor nanoparticles (NPs) have attracted much attention in recent years due to novel optical, electrical and mechanical properties; resulting from quantum confinement effects compared with their bulk counterparts [1]. Undoped ZnO is an important transparent conductive oxide material; found naturally as n type due to the native defects such as oxygen deficiency and zinc excess and due to its direct energy gap, large excitation binding energy at room temperature, wurtzite structure, chemical stability, good transparency and high electron mobility. It can be used in a variety of applications [2–4], such as photocatalyst, varistor and photodetectors [5]. To deposit the ZnO NPs films, various methods have been employed such as pulsed laser ablation in liquid, spray pyrolysis, reactive and ion-assisted evaporation, sputtering, electrochemical deposition, sol–gel processing, arc discharge and spray pyrolysis [6]. Recently, ZnO nanowires arrays were used as antireflection coating to improve the efficiency of silicon solar cells due to its large band gap and large surface area [7]. Here, we have grown and characterized of ZnO NPs films by thermal oxidation of Zn NPs. The photovoltaic properties of *n*-ZnO/*p*-Si heterojunction solar cells were studied as function of oxidation temperature.

2 Experimental

Preparation of ZnO NPs was carried out in three steps using the same procedure used in Ref. [8]. Colloidal suspension of zinc hydroxide was formed by immersing 99 % purity metallic zinc pellet into 35 % hydrogen peroxide solution at temperatures between (20 and 60) °C. The zinc hydroxide colloidal suspension was sprayed onto clean silicon wafers

Table 1 Spray conditions and nozzle specifications

Spray parameter	Optimum values/item
Nozzle	Glass
Nozzle—substrate distance	28 cm
Carrier gas	Compressor air
Spray period	5 on–10 off
Flow rate	3 mL min^{-1}
Nozzle diameter	0.2 mm
Substrate temperature	80 °C

Table 2 Grain size and lattice constants of ZnO NPs film at 300 K

Oxidation temperature (°C)	FWHM (°) for (100) plane	2θ (°) (100) plane	Grain size (nm) of (100) plane	a (nm)	c (nm)	Strain e_{aa}
300	0.51330	30.79	16.06	0.332	0.507	0.024
400	0.32170	30.95	25.05	0.3328	0.509	0.024
500	0.29169	30.97	28.26	0.3328	0.507	0.0242

and quartz substrates (see Table 1). The temperature of substrates was maintained at 80 °C. The sprayed films were oxidized in the temperature range (300–500) °C in static air using tube furnace to form ZnO NPs. The 500-μm-thick (111)-oriented mirrorlike CZ p-type silicon of (1–3) Ω cm resistivity and 1 cm^2 area were used as substrates in this study. Before spraying, the silicon wafers were cleaned using RCA method, while the quartz slides were cleaned by acetone followed by rinsing them in distilled water. Ohmic contacts were made on ZnO NPs film and silicon substrate by depositing of aluminum films through special mask using thermal resistive technique under vacuum pressure of 10^{-6} torr. The structure of ZnO NPs was investigated using X-ray diffraction with CuKα radiation ($\lambda = 0.154$ nm) and the 2θ in the range of 20°–60°. The optical transmittance of ZnO film deposited on quartz substrate was measured using UV–Visible spectrophotometer (Metratech) in wavelength range of (300–900) nm. Photoluminescence investigation was carried out using a He–Cd laser (LABRM-HR) spectrophotometer. The morphology of the NPs was characterized by atomic force microscopy (AFM) (CSPM-5000) and scanning electron microscopy (SEM) (VEGA TE SCAN).

The C–V characteristics were studied using LCZ system (Fluke PM 6306) at a reverse bias in the range of (0–6) V at a frequency of 100 kHz. The spectral responsivity was measured with aid of calibrated monochromatic (type Joban model 1746) in the range of (400–900) nm. Solar simulator was used to measure the photovoltaic characteristics of ZnO/Si solar cells at $AM_{1.5}$ (100 mW cm^{-2}).

3 Results and discussion

3.1 Structural properties

The ZnO film oxidized at 200 °C was amorphous structure with a spectrum of no specific peak due to the insufficient temperature for arranging the molecules in a crystalline form. By increasing the oxidation temperature to 300 °C, the grown films showed polycrystalline structure with hexagonal wurtzite phase and exhibited sharp peaks at

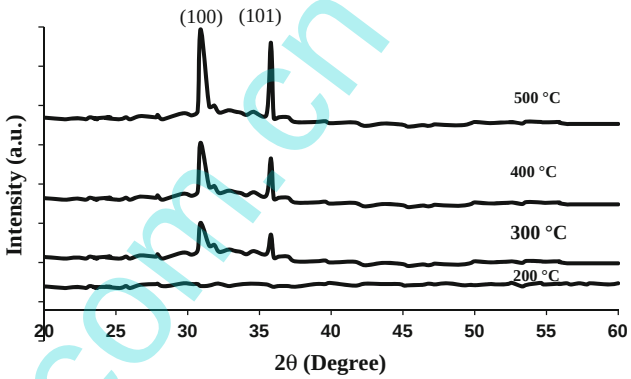

Fig. 1 XRD patterns of ZnO NPs films at various oxidation temperatures

31.2° and 35.9° which corresponding to reflection (100) and (101) planes, respectively, which are agree well with the reported standard values (JCPDS no-36-1451 data). The reflection peak of (100) plane of the film oxidizes at 300, 400 and 500 °C is shifted slightly toward larger values due to the tensile stress in ZnO NPs along the a-axis as shown in Table 2. The tensile stress could have resulted from to the oxygen vacancies in the lattice of ZnO crystallites in the film [9]. The reflection peaks (110) and (101) clearly became sharper with increasing intensity of peaks with oxidation temperature, indicating an enhancement in the film stoichiometry and crystallinity. Furthermore, the oxidation at higher temperature provided energy of particles to improve the mobility that could reduce the structural defects in the ZnO NPs [10]. No peaks related to Zn impurities and/or non-stoichiometric phase are detected in the XRD spectra, indicating the high purity of the product (Fig. 1).

The grain size of ZnO NPs is estimated using Scherrer–Debye formula (X-ray line broadening). Table 2 lists the values of grain size of (100) plane, lattice constants and strain. The calculated lattice constants of ZnO NPs are close to those for the bulk ZnO ($a_o = 0.3246$ and $c_o = 0.5206$ nm at 300 K) [11]. Table 2 revealed that the grain size of the of ZnO NPs increases with oxidation

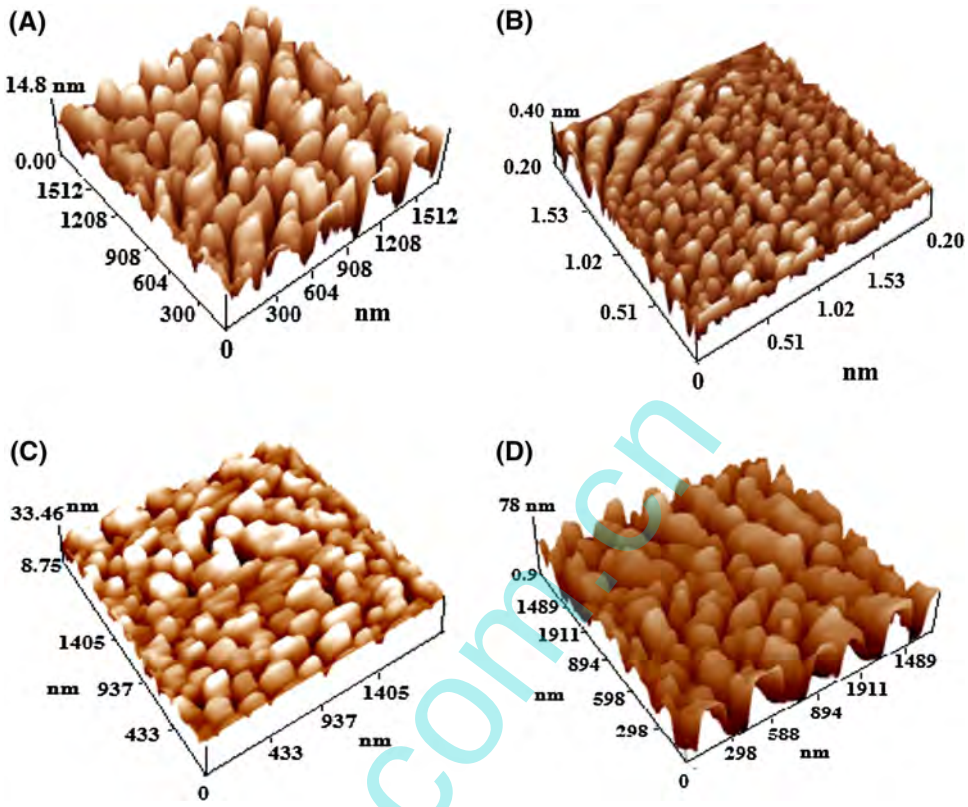

Fig. 2 3D AFM images ZnO NPs oxidized at **a** 200 °C, **b** 300 °C, **c** 400 °C and **d** 500 °C

Table 3 Grain size and root mean square of surface roughness obtained from AFM data

Oxidation temperature (°C)	Average grain size (nm)	Root mean square (RMS) (nm)
200	72.74	1.35
300	84.20	2.3
400	90.37	3.1
500	95.86	5.3

temperature. This result is agree well with data in Refs. [9, 12]. At high oxidation temperature, the small crystallites coalesce together and make larger crystallites.

The coalescence process causes major grain growth resulting in porosity and surface roughness [13]. The value of e_{aa} is positive meaning the existence of tensile stress along *a*-axis of ZnO NPs film. Figure 2 shows the 3D AFM images of the ZnO NPs oxidized at various temperatures. It is clear that the grain size and direction of growth are strongly dependent on the oxidation temperature. The AFM images confirm this finding and shows spherical (rounded) ZnO NPs when prepared at high oxidation temperatures. The grown NPs have good dispersibility, and the grains are homogenous and aligned vertically. The NPs prepared at higher oxidation temperature aggregate and formed larger particles.Using special software, the values of root mean square surface roughness and average grain size are estimated and summarized in Table 3.

It is seen from this Table 3 that the average grain size and roughness increase with oxidation temperature due to the major grain growth [13]. The average grain size of ZnO NPs obtained from XRD measurements is smaller than that estimated from AFM measurements, indicating a probable grains aggregate of many crystallites. The generating of stress in ZnO NPs has increased the FWHM value which affected the calculation of grain size. These results agree well with data in literatures [14, 15].

3.2 SEM investigation

SEM images of ZnO NPs prepared at 300, 400 and 500 °C given in Fig. 3 revealed that the particles exhibit irregular morphology. It is obvious that the ZnO NPs are not entirely spherical in shape and are not distributed uniform and have different particle sizes due to agglomeration of small crystallite. The SEM micrograph showed formation of non-uniform and different shapes particles, cubic and spherical NPs were observed. This is possible since the method of preparation allows stacking and agglomeration of initial single particles [16]. Higher oxidation temperature permitted the formation larger ZnO NPs grain size. Complex ZnO nanostructures such as flakelike structures were noticed as shown in the inset of Fig. 3a, and also this

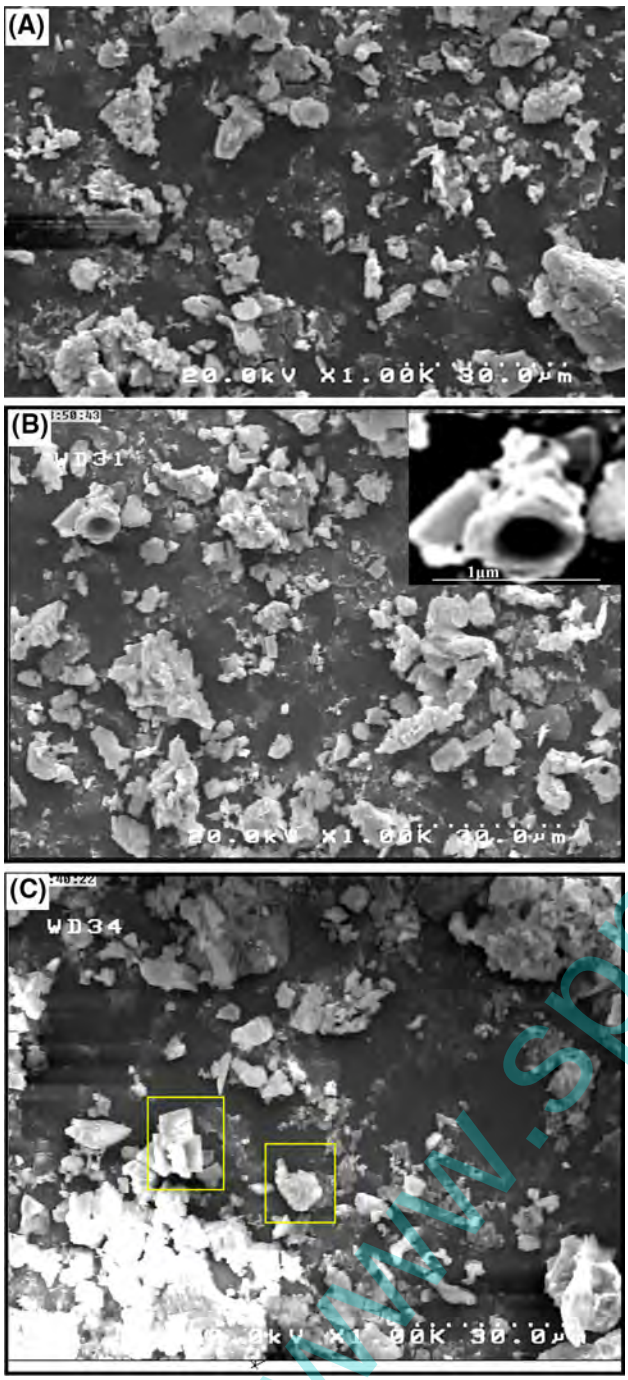

Fig. 3 SEM images of ZnO NPs oxidized at **a** 300 °C, **b** 400 °C and **c** 500 °C. *Inset* is the flakelike structure

complex structure was found for ZnO nanostructure formed at $T_{ox} = 500$ °C as shown in rectangles of Fig. 3b.

3.3 Optical properties

In order to investigate the effect of oxidation temperature on the optical properties of the ZnO NPs films, photoluminescence measurement was taken over the wavelength

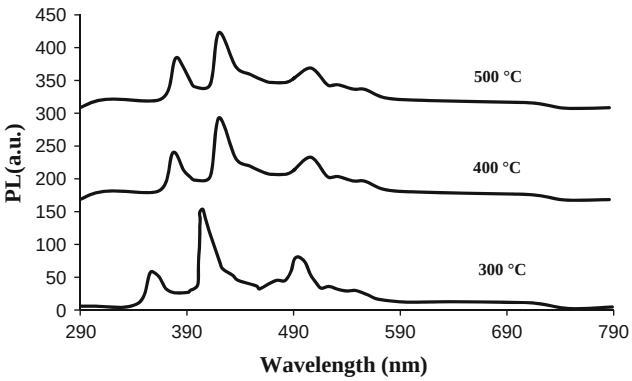

Fig. 4 Room temperature PL spectra of ZnO NPs

range of (290–790) nm as shown in Fig. 4. PL spectrum of ZnO NPs oxidized at 300 °C revealed three specific peaks located at 373.1, 425 and 506 nm. The origin of first and third peaks is the recombination of confined excitons and oxygen antisite, respectively. The second peak (green emission) is ascribed to the electronic transition from defect level, corresponding to high concentration of zinc interstitials to the valence band and due to singly ionized oxygen vacancies [17]. When the oxidation temperature increased to 400 °C, three peaks at 377, 427 and 513 nm were observed. PL spectrum of ZnO NPs oxidized at 500 °C showed the presence of three peaks located at 380, 424.6 and 513.6 nm. The PL spectra show an emission peak at around 373 shifts to longer wavelength as oxidation temperature increases. This shifting in position (band gap energy) is probably related to the formation of coarser grains and attributed to the quantum—confinement effect and also due to the residual stress along a-axis of ZnO originated from lattice distortion [18]. Increasing the oxidation temperature leads to decreasing oxygen and zinc vacancies and increasing the oxygen antisite (O_{Zn}). Increasing the oxidation temperature further has increased the intensity of UV peak, but decreasing it for the green and violet emission peaks. The intensity increase of the UV peak indicates an improvement in the crystalline nature of the grown ZnO NPs film. In addition to these three peaks, other small peaks are also found in the visible region of PL spectra, probably related to the defects levels in ZnO NPs.

The decrease in green and violet emission peaks intensity is due to the reduction of point defects, such as oxygen vacancy and zinc interstitials presented in the synthesised ZnO NPs film [19]. These PL results are consistent with those reported in Ref. [20]. Figure 5 shows the optical transmittance spectra in the wavelength range of (300–900) nm of fresh ZnO NPs films deposited on quartz substrate at different oxidation temperatures. The average optical transmittance of the films oxidized at 300 °C decreased from 70 to 65 % when the films were oxidized at

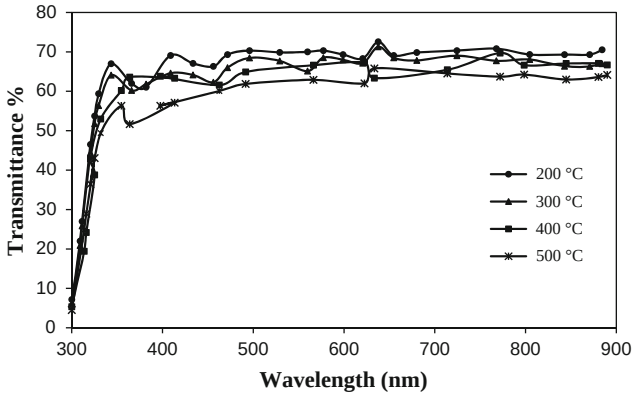

Fig. 5 Transmittance of ZnO films oxidized at different temperatures

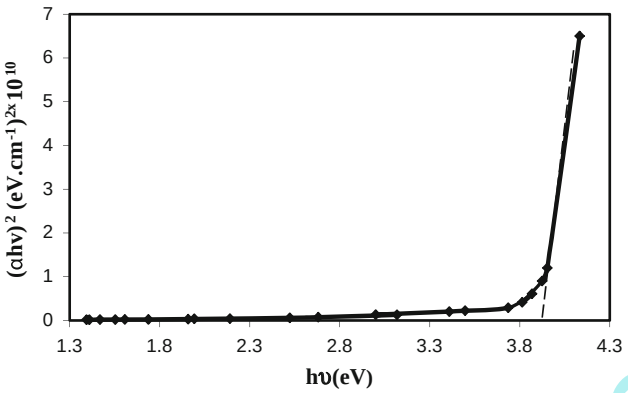

Fig. 6 $(\alpha h\nu)^2$ as function of photon energy of ZnO NPs thin films oxidized at 500 °C

Table 4 Energy gap of ZnO NPs as function of oxidation temperature

Oxidation temperature (°C)	Energy gap (eV)
400	3.96
300	3.82
400	3.78
500	3.72

500 °C. This decrease is due to the coalesce process in grain boundaries [21]. All synthesised films exhibited a sharp absorption edge.

Figure 6 shows a linear dependence plot of $(\alpha h\nu)^2$ against $(h\nu)$, indicating a direct transition ZnO NPs semiconductor films [22]. The band gap E_g is determined by extrapolating the linear portion of the $(\alpha h\nu)^2$ curve toward the $(h\nu)$ axis. The values of energy gap of the grown ZnO film, given in Table 4 shows larger energy gap than that of the bulk ZnO (3.7 eV at room temperature) due to quantum

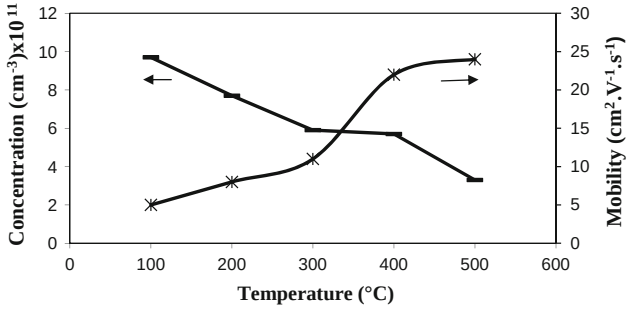

Fig. 7 Carrier concentration and mobility as a function of oxidation temperature

confinement. Higher oxidation temperature decreased the energy gap of the film due to the formation of larger grain size.

3.4 Electrical properties

Figure 7 shows a plot for mobility and carrier concentration versus oxidation temperature. Hall measurement confirms that ZnO is *n* type and excess electrons are considered to be introduced by the presence of Zn interstitials and/or oxygen vacancies [23]. Figure 7 shows an increasing of oxidation temperature leads to reduction of the carrier concentration, as a considerable quantity of oxygen is chemisorbed during the oxidation processes a considerable quantity of oxygen is chemisorbed. Chemisorbed oxygen acts as a strong trap for free carriers which play important role in decreasing the electron concentration [22].

Figure 7 also shows that increasing of the carrier mobility with oxidation temperature due to the decreasing of structural defects at grain boundary and/or grain growth.

3.5 Heterojunction characteristics

3.5.1 Capacitance–voltage measurement

Figure 8 shows a linear relationship between C^{-2} and bias voltage of *n*-ZnO/*p*-Si heterojunction solar cell oxidized at 500 °C. This linear relationship of C^{-2} with bias voltage suggests abrupt-type junctions. The interception of C^{-2} curve with voltage axis gives the diffusion potential V_{bi}. The estimated values of V_{bi} for a range of oxidation temperatures are listed in Table 5. The diffusion potential increases slightly with oxidation temperature. The values of V_{bi} are close to those for ZnO/Si heterojunctions prepared by other methods [21, 24, 25].

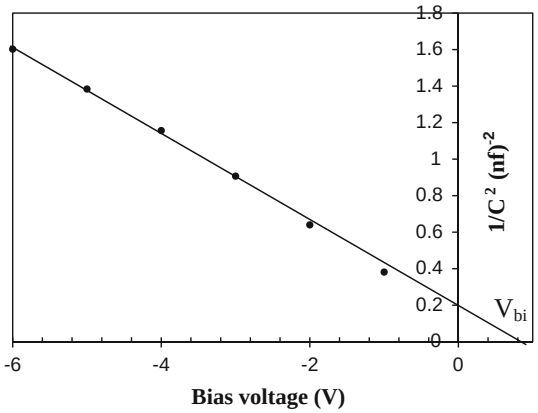

Fig. 8 C^{-2} versus bias voltage plot for *n*-ZnO NPs/*p*-Si solar cell oxidized at 500 °C

Table 5 Built-in potential as function of oxidation temperature

Oxidation temperature (°C)	Built-in potential (V)
300	0.60
400	0.63
500	0.65

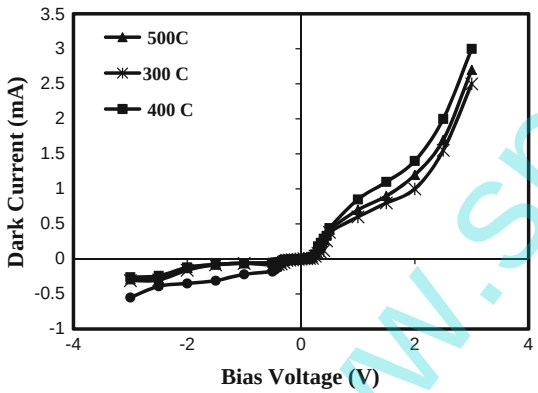

Fig. 9 Dark *I–V* characteristics of heterojunctions

3.5.2 *Current–voltage measurement*

Figure 9 shows the dark current–voltage (*I–V*) characteristics at forward and reverse directions. From *I–V* plot, the saturation current and ideality factor calculated as function of oxidation temperature are listed in Table 6. Table 6 shows large values of ideality factor suggesting the domination of recombination process in these devices. These values describe ideality factors in the junction region and/or at the junction of ZnO–Si [26]. The mismatch lattice constant affects also the junction characteristics and ideality factor. The ideality was decreasing with the oxidation

Table 6 Values of ideality factor and saturation current

Oxidation temperature (°C)	Ideality factor	I_s (μA)
300	2.8	2.7
400	2.5	1.35
500	2	2.25

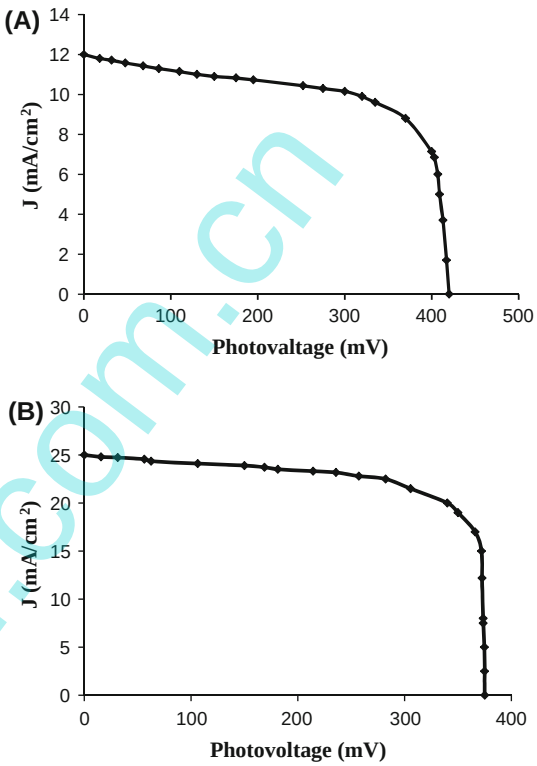

Fig. 10 Illuminated *J–V* characteristics of ZnO NPs/*p*-Si oxidized at **a** 400 °C and **b** 500 °C

temperature rise due to the reduction in structural defects at interface. The illuminated *J–V* of ZnO/Si heterojunction solar cells prepared at oxidation temperature of 400 and 500 °C are presented in Fig. 10.

Enhancement in the photovoltaic properties was noticed at higher oxidation temperature due to reduced imperfections and increased of ZnO NPs grain size, which in turns increases the short circuit current density. The diffusion of adsorbed oxygen in bulk ZnO film at high oxidation temperature resulted in an increasing the free carriers. The best solar cell gave $J_{sc} = 25$ mA cm^{-2}, $V_{oc} = 375$ mV, FF = 0.72, and $\eta = 6.79$ %. The photovoltaic parameters of the ZnO/Si solar cells prepared by oxidation of Zn at different oxidation temperatures are given in Table 7. The short current density increased significantly due to suppressing the light reflectivity by ZnO NPs [7].

The present value of conversion efficiency is very close to that of nanostructured ZnO:Al/Si solar cell prepared by successive chemical solution [27]. The photovoltaic

Table 7 Photovoltaic parameters of ZnO/Si solar cells at 100 mW/cm^2

Oxidation temperature (°C)	J_{SC} (mA cm^{-2})	V_{OC} (mV)	V_m (mV)	J_m (mA cm^{-2})	FF	η (%)
300	1.2	359	210	0.7	0.32	0.13
400	12	420	370	8.8	0.64	3.25
500	25	375	340	20	0.72	6.79

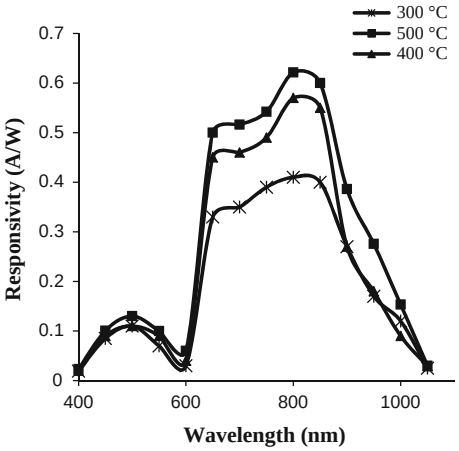

Fig. 11 Spectral responsivity plot for *n*-ZnO NPs/*p*-Si solar cells

parameters of solar cells were measured after 3 months of storing in normal ambient, and no significant degradation in their characteristics was noticed.

3.5.3 Spectral responsivity of n-ZnO/p-Si solar cells

Figure 11 reveals the photosensitivity of ZnO/Si solar cells oxidized at different temperatures. As presented in Fig. 11, the photosensitivity of all solar cells is basically composed of near band edge absorption of Si substrate at wavelengths range of (600–850) nm and near band edge absorption of ZnO NPs at wavelengths range 300–600 nm. Solar cell oxidized at 500 °C gave the maximum responsivity. The peak of the first response region was located at wavelength of around 590 nm wavelength (ZnO layer) with responsivity of 0.13 AW^{-1}, while that of the second response was around 800 nm wavelength (Si wafer) with responsivity of 0.62 AW^{-1}. The average photosensitivity of the best solar cell at the wavelength between 400 and 800 nm was 0.27 AW^{-1}. The photosensitivity improvement of the solar cells in the wavelengths range of 300–600 nm can be ascribed to the large optical band gap of ZnO NPs as well as the morphology of ZnO NPs layer may be played an important in reducing the reflectivity [28].

4 Conclusions

Low-cost, simple and efficient method was used to fabricate high-efficiency *n*-ZnO NPs/*p*-Si solar cells. Structural, optical and electrical properties of ZnO NPs films were investigated at different values of oxidation temperature. Solar cells fabricated at optimum oxidation temperature of 500 °C gave $J_{sc} = 25$ mA cm^{-2}, $V_{oc} = 375$ mV and $\eta = 6.72$ %. The photosensitivity of solar cells, under study, composed basically of near band edge absorption of Si substrate at wavelengths range of (600–850) nm and near band edge absorption of ZnO NPs at wavelength range of 300–600 nm. No remarkable change in the solar cells characteristics was observed after being stored under ambient conditions. Oxidation of zinc NPs thin film suggests wider applications of low-cost heterojunction solar cells.

References

1. C. Chen, B. Yu, P. Liu, J. Lue, L. Wang, J. Ceram. Process. Res. **12**, 420–425 (2011)
2. J. Yoo, J. Lee, S. Kim, K. Yoon, I. Park, S. Duugel, B. Karuuagarn, D. Mangalarag, J. Yi, Thin Solid Films **480–481**, 213–217 (2005)
3. S. Shariffudin, M. Salina, S. Herman, J. Trans. Electr. Electron. Mater. **13**, 102–105 (2012)
4. P. Baviskar, P. Nikam, S. Gargote, A. Ennaoui, B. Sankapal, J. Alloy. Compd. **551**, 233–242 (2013)
5. X. Liu, Z. Jin, Z. Liu, K. Yu, S. Bu, J. Appl. Surf. Sci. **252**, 8668–8672 (2006)
6. X. Hao, J. Ma, D. Zhang, T. Yang, H. Ma, Y. Yang, C. Cheng, J. Huang, Appl. Surf. Sci. **138**, 137–142 (2001)
7. X. Yu, D. Wang, D. Lri, D. Yang, Nano Scale Res. Lett. **7**, 306–311 (2012)
8. Z. Ji, S. Zhao, C. Wang, K. Liu, Mater. Sci. Eng. B **117**, 63–66 (2005)
9. Z. Fang, Z. Yan, Y. Tan, X. Liu, Y. Wang, Appl. Surf. Sci. **241**, 303–308 (2005)
10. G. Patwari, P. Kalita, Nanosci. Nanotechnol. Int. J. **4**, 13–17 (2012)
11. M. Gondal, Q. Drmosh, Z. Yamani, T. Saleh, Appl. Surf. Sci. **256**, 298–302 (2009)
12. D. Raoufi, T. Raoufi, Appl. Surf. Sci. **255**, 5812–5817 (2009)
13. F. Porter, *Zinc Handbook: Properties, Processing, and Use in Design* (CRC Press, Boca Raton, 1991)
14. T. Rao, M.C. Kumar, V. Ganesan, Indian J. Phys. **85**, 1381 (2011)
15. Y. Lee, S. Hu, W. Water, K. Tiong, Z. Feng, Y. Chen, J. Hung, J. Lee, C. Huang, J. Shen, M. Cheng, J. Lumin. **120**, 148 (2009)
16. S. Mondal, K. Kanta, P. Mitra, Mater. Res. **16**, 94 (2013)
17. Q. Wang, D. Zhang, Z. Xue, X. Hao, Appl. Surf. Sci. **201**, 123 (2002)
18. Y. Chien, S. YaoHu, W. Water, K. Tiong, Z. Feng, Y. Chen, J. Huang, J. Lee, C. Huang, J. Shen, M. Cheng, J. Lumin. **129**, 148–152 (2009)

19. E. Shim, H. Kang, J. Kang, J. Kim, S. Lee, Appl. Surf. Sci. **186**, 474 (2002)
20. R. Orimi, Opt. Mater. **35**, 657 (2013)
21. M. Ohyama, H. Kozuka, T. Yoko, Thin Solid Films **306**, 78 (1997)
22. M. Bouderbala, S. Hamzaoui, M. Adnane, T. Sahraoui, M. Zerdali, Thin Solid Films **517**, 1572 (2009)
23. V. Khranovskyy, A. Ulyashin, G. Lashkarev, B. Svensson, R. Yakimova, Thin Solid Films **516**, 1396 (2008)
24. H. Afify, S. El-Hefnawi, A. Eliwa, M. Abdel-Naby, N. Ahmed, Egypt J. Solids **28**, 243 (2005)
25. R.A. Ismail, A. Al-Naimi, A.A. Al-Ani, Semicond. Sci. Technol. **23**, 075030 (2008)
26. R.A. Ismail, D.N. Raou, D.F. Raouf, J. Optoelectron. Adv. Mater. **8**, 1443 (2006)
27. O. Lupan, S. Shishiyanu, V. Ursaki, H. Khallaf, L. Chow, T. Shishiyanu, V. Sontea, Sol. Energy Mater. Sol. Cells **93**, 1417 (2009)
28. C. Chen, P. Lin, L. Chen, M. Ke, Y. Cheng, J. Huang, Nanotechnology **20**, 245204 (2009)